



Nanoparticulate Ru on TiO₂ exposed the {1 0 0} facets: Support facet effect on selective hydrogenation of benzene to cyclohexene

Gongbing Zhou*, Lan Jiang, Daiping He

Chongqing Key Laboratory of Green Synthesis and Applications, College of Chemistry, Chongqing Normal University, Chongqing 401331, China



ARTICLE INFO

Article history:

Received 23 September 2018

Revised 19 November 2018

Accepted 26 November 2018

Keywords:

Ruthenium

TiO₂ facet

Benzene

Cyclohexene

Hydrogenation

ABSTRACT

Support facet effect of supported metal catalysts for conversion of environmentally toxic feedstock to value-added product is challenging but of significant importance for the understanding of the reaction mechanism and accordingly rational design of newly high-efficient catalytic materials. We report here the effect of the exposed degree of TiO₂ {1 0 0} facets, which was facilely tuned by hydrothermal temperature, on benzene selective hydrogenation to cyclohexene over TiO₂-supported nanoparticulate Ru catalysts. It is found that the Ru/TiO₂ catalyst exposed the most {1 0 0} facets exhibited slightly lower intrinsic activity, but unexpectedly highest selectivity towards cyclohexene (initial selectivity of 93%). A positively linear correlation between the initial selectivity to cyclohexene and the amount of surface OH groups on the Ru/TiO₂ catalysts, which was determined by the exposed degree of TiO₂ {1 0 0} facets, was identified. This linearity rationalizes the selectivity enhancement of the Ru/TiO₂ catalyst exposed more {1 0 0} facets since the surface OH groups functioned in increasing the hydrophilicity of the catalysts, decreasing the type of adsorption sites of cyclohexene, and blocking the chemisorption sites of cyclohexene.

© 2018 Elsevier Inc. All rights reserved.

1. Introduction

Design of TiO₂ with specific crystal facets has been intensively studied since the surface atomic coordination and configuration, which essentially affect its catalytic performance, can be well tuned by crystal facet control [1–3]. For instance, owing to a cooperative mechanism of surface atomic structure and surface electronic structure, the photoreactivity of {0 0 1}, {1 0 1}, and {0 1 0} facets of anatase TiO₂ crystals in photooxidation and photoreduction reactions was proved to be {0 1 0} > {1 0 1} > {0 0 1} [1]. Among the three natural phases of TiO₂ (anatase, rutile, and brookite), anatase is most intensively studied and applied in catalysis and photocatalysis owing to its higher stability in strongly basic solution or when the particle size is below 11 nm [4]. To investigate the facet effect of anatase TiO₂, synthesis of TiO₂ crystals with specific facets is highly required. Until now, the low-index facets ({0 0 1} [1,5], {1 0 1} [1,5], {1 0 0} [6], {0 1 0} [1], and {1 1 0} [7]) and high-index facets ({1 0 3}, {1 0 5}, {1 0 6}, {1 0 7}, {2 0 1}, {3 0 1}, and {4 0 1}) [4] of anatase crystals have been synthesized by wet-chemistry route, epitaxial growth, gas oxidation route, crystallization transformation, and topotactic transformation. For

the most studied {0 0 1}, {1 0 1}, and {1 0 0} facets, although the stability decreased in the sequence of {0 0 1} > {1 0 1} > {1 0 0} since the relative surface energies increased on the contrary, the {1 0 0} facets were more active and consequently showed higher catalytic activity than the other two facets as predicted by DFT calculations [8].

In contrast, studies regarding with the facet effect of TiO₂ when serving as a support for metal nanoparticles (NPs) are rare [9–11], while it is remarkably important from both scientific and technological perspectives as it may provide new tuning factors or mechanisms to improve the catalytic performance of supported metal catalysts other than the known physical effect of support and “strong metal-support interaction (SMSI)” [12–16]. Different facets with diverse surface atomic configurations displayed unique interactions with metal NPs, thereby exhibiting different catalytic performances. Sui et al. demonstrated that the Pt atoms selectively deposited on TiO₂ with a proper percentage of exposed {0 0 1} and {1 0 1} facets were more reactive than those on TiO₂ with dominated {1 0 1} facets or {0 0 1} facets in sunlight-driven hydrogen production from water splitting, owing to the enhanced “surface heterojunction” effect between {0 0 1} and {1 0 1} facets on the former [9]. Cao et al. reported that the Pd NPs enclosed by {1 0 0} or {1 1 1} facets dosed on TiO₂ (0 0 1) crystal plane exhibited higher activity than which on TiO₂ (1 0 1) plane in oxygen activation reaction [10]. Therefore, the selection of the support facets

* Corresponding author.

E-mail address: gbzhou@cqnu.edu.cn (G. Zhou).

can offer a new tuning parameter to regulate the catalytic performance of metal NPs.

These leading works inspire us to explore the facet effect of TiO_2 when serving as a support for Ru NPs on other industrially important reactions, such as the conversion of environmentally toxic feedstock to value-added product (benzene selective hydrogenation to cyclohexene) addressed in the present work. The tetragonal faceted-nanorods of anatase TiO_2 single crystals with different exposed degrees of highly reactive $\{1\ 0\ 0\}$ facets were firstly synthesized by hydrothermal route at different temperatures (433–473 K), and then the Ru/ TiO_2 catalysts were prepared by a facile wetness impregnation–chemical reduction method. We identified that the hydrothermal temperature is essential to the exposed degree of $\{1\ 0\ 0\}$ facets, and the temperature to expose the most $\{1\ 0\ 0\}$ facets is 453 K. Meanwhile, O1s X-ray photoelectron spectroscopic (XPS) spectrum, Fourier transform infrared spectroscopy (FTIR), and water contact angle demonstrated that the hydrophilicity of the Ru/ TiO_2 catalysts was in line with the exposed degree of TiO_2 $\{1\ 0\ 0\}$ facets. In the selective hydrogenation of benzene to cyclohexene, the Ru/ TiO_2 -453 catalyst exhibited higher selectivity than the Ru/ TiO_2 -433, Ru/ TiO_2 -443, and Ru/ TiO_2 -473 catalysts prepared in the same manner. An excellent linear correlation between the cyclohexene selectivity and the hydrophilicity of these catalysts was confirmed, which rationalizes the significant impact of TiO_2 facets on selectivity enhancement in selective hydrogenation of benzene over Ru/ TiO_2 catalysts.

2. Experimental

2.1. Preparation

$\text{RuCl}_3 \cdot 3\text{H}_2\text{O}$ was purchased from Adamas. P25 TiO_2 was supplied by Degussa. Benzene was purchased from Sigma-Aldrich. Other unspecified chemicals were provided by Sinopharm Chemical Reagent. All chemicals are analytical grade (A.R.). The gases were purchased from Chongqing Ruike Gas Co.

The fabrication of the Ru/ TiO_2 catalysts is graphically illustrated in Scheme 1. Firstly, TiO_2 crystals exposed different degrees of $\{1\ 0\ 0\}$ facets were synthesized according to the strategy developed by Li et al. with some modifications [6]. Specifically, 4 g P25 TiO_2 and 80 ml of NaOH aqueous solution (10 M) were mixed and transferred to a 200 ml-capacity Teflon-lined stainless steel autoclave. The autoclave was sealed and hydrothermally treated at 393 K for 24 h. After cooling down to room temperature, the white precipitates were separated and washed with deionized water until the pH of approximate 10.5, producing Na-titanate intermediates. Then, 2 g of the wet intermediates were dispersed into 80 ml of deionized water and transferred to a 100 ml-capacity Teflon-lined stainless steel autoclave. The autoclave was sealed and hydrothermally treated at 433, 443, 453, and 473 K for 24 h, respectively. After cooling down to room temperature, the white precipitates were separated by centrifugation and washed with deionized water until neutrality, and dried at 333 K for 10 h. The

obtained products were labeled TiO_2 - x , where x represents the temperature of the second hydrothermal treatment step.

The above TiO_2 samples were then used as supports to prepare the Ru/ TiO_2 catalysts by the wetness impregnation–chemical reduction strategy. 0.5 g of the as-prepared TiO_2 sample was dispersed in 10 ml of deionized water. 1.5 ml of $\text{RuCl}_3 \cdot 3\text{H}_2\text{O}$ aqueous solution (0.40 M) was added. After stirring for 3.5 h, 1.5 ml of KBH_4 aqueous solution (1.58 M) was added dropwise. The nominal Ru loading was 10.7 wt% for the catalysts. The solids were washed with deionized water until inexistence of Cl^- (AgNO_3 test). The obtained catalysts were denoted as Ru/ TiO_2 - x according to the kind of the respective TiO_2 support. For comparison, the Ru/ Al_2O_3 , Ru/ SiO_2 , Ru/ CoO , Ru/ NiO , Ru/ CuO , and Ru/ ZnO catalysts were also prepared via the same strategy.

2.2. Catalytic evaluation

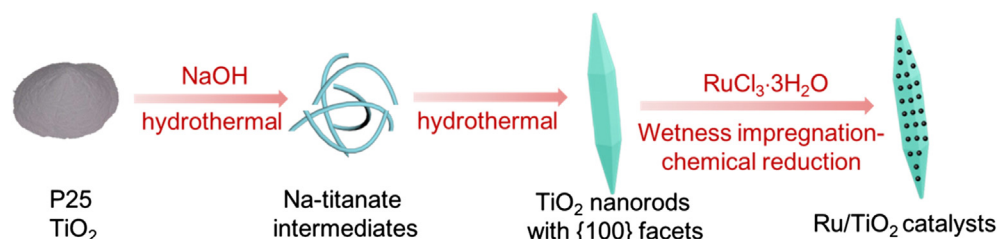
Selective hydrogenation of benzene to cyclohexene was tested in a 250 ml-capacity autoclave with a mechanical stirrer. After introducing 0.5 g of catalyst, 5.0 g of $\text{ZnSO}_4 \cdot 7\text{H}_2\text{O}$, 50 ml of H_2O , and 25 ml of benzene, the autoclave was sealed and purged with H_2 . The reaction conditions are temperature of 413 K, H_2 pressure of 5.0 MPa, and stirring speed of 1000 rpm, which are typical for the selective hydrogenation of benzene [12,17–21]. The product was analyzed by a SC-3000B gas chromatograph with a thermal conductivity detector (TCD) and a PEG-20M packed column. The catalysts were tested in duplicate, and the results agreed within $\pm 2\%$.

As the benzene conversion, the cyclohexene selectivity, and the cyclohexene yield changed with reaction time (t), the turnover frequency (TOF) of benzene and the initial selectivity towards cyclohexene (S_0), which were absolutely fair for all the catalysts, were used to compare the intrinsic activity and selectivity, respectively. For the calculation of the TOF, the initial weight-specific activity (r_0), that is, the reacted millimoles of benzene per gram of the catalyst per minute at the beginning of the reaction, was acquired first by the approach reported by Hu et al. [22]. Precisely, the polynomial equation acquired by fitting the experimental curve of benzene content and reaction time was differentiated, and the r_0 was obtained by using zero to replace t . The TOF was calculated according to the formula raised in our previous work [23]. For the S_0 , the linear correlation of cyclohexene selectivity and t was fitted, and the intercept is S_0 .

3. Results and discussion

3.1. Texture and morphology of TiO_2 nanorods

Table 1 lists the physicochemical parameters of the TiO_2 samples. The N_2 adsorption–desorption isotherms of the samples (Fig. S1) all belonged to type IV with H3 hysteresis loop. According to Table 1, a sharp decrease of the multipoint Brunauer–Emmett–Teller surface area (S_{BET}) and the pore volume (V_{pore}) was observed when the hydrothermal temperature was elevated from 433 to



Scheme 1. Schematic illustration of the synthesis of TiO_2 single crystals with dominated $\{1\ 0\ 0\}$ facets-supported Ru catalysts.

Table 1
Physicochemical properties of TiO₂ and the Ru/TiO₂ catalysts.

Sample	Ru loading ^a (wt%)	Dispersion ^b (%)	S _{BET} (m ² g ⁻¹)	d _{pore} (nm)	V _{pore} (cm ³ g ⁻¹)
TiO ₂ -433	n.a. ^c	n.a.	35	8.2	0.19
TiO ₂ -443	n.a.	n.a.	6	22.5	0.06
TiO ₂ -453	n.a.	n.a.	7	23.1	0.05
TiO ₂ -473	n.a.	n.a.	3	30.5	0.04
Ru/TiO ₂ -433	10.5	25.8	90	5.9	0.26
Ru/TiO ₂ -443	10.4	24.9	14	17.9	0.09
Ru/TiO ₂ -453	10.5	26.2	16	13.7	0.08
Ru/TiO ₂ -473	10.6	25.3	12	18.6	0.08

^a Determined by ICP-AES.

^b Dispersion of Ru determined by CO chemisorption.

^c n.a.: not applicable.

443 K, while further elevation of the temperature induced slight impact on S_{BET} and V_{pore}. For the average pore diameter (d_{pore}), it increased gradually accompanying the elevation of the hydrothermal temperature. The powder X-ray diffraction (XRD) patterns of the TiO₂ samples as well as the Na-titanate intermediate are presented in Fig. 1. The peaks in Fig. 1a–d at 2θ of 25.4°, 37.0°, 37.9°, 38.7°, 48.2°, 54.1°, 55.2°, 62.1°, 62.7°, and 68.9° are respectively ascribed to the (1 0 1), (1 0 3), (0 0 4), (1 1 2), (2 0 0), (1 0 5), (2 1 1), (2 1 3), (2 0 4), and (1 1 6) crystal planes of anatase TiO₂ (tetragonal, JCPDS 21-1272), showing that the Na-titanate intermediate was transferred into an anatase phase after hydrothermal treatment.

As a representative, the scanning electron microscopy (SEM) image of the TiO₂-453 sample is showed in Fig. 2a. It indicated a nanorod shape enclosed by four tetragonal facets, and the adjacent facets of the nanorod were perpendicular (inset in Fig. 2a). The transmission electron microscopy (TEM) images with corresponding selected-area electron diffraction (SAED) patterns (Fig. 2b and c) revealed more structural information of the TiO₂ nanorod. The SAED pattern in Fig. 2b revealed that the [0 0 1] and [1 0 0] directions are perpendicular, which is in line with the schematic model of anatase TiO₂ nanorod enclosed by {1 0 0} facets along the [0 1 0] direction (inset in Fig. 2b). The high-resolution TEM (HRTEM) image taken from the rectangle revealed two sets of lattice fringes with spacings of 3.52 and 2.43 Å, attributable to (1 0 1) and (1 0 3) planes of anatase, respectively. To confirm the exposed facets, the nanorod along the [0 2 1] direction was showed in Fig. 2c. The width of the nanorod along this direction is 1.4 times as that along the [0 1 0] direction. Both the SEAD pattern and HRTEM image inserted of Fig. 2c demonstrated that the TiO₂ nanorod had a

single-crystalline structure of anatase exposed with {1 0 0} facets, matching well with the schematic model enclosed by {1 0 0} facets along the [0 2 1] direction (inset in Fig. 2c). Based on the above analysis, the exposed lateral facets of the as-prepared TiO₂ nanorods are mainly the {1 0 0} facets, in agreement with the observation of Li et al. [6].

3.2. Physicochemical characteristics, morphology, and microstructure of the Ru/TiO₂ catalysts

With the as-synthesized TiO₂ samples, we prepared the Ru/TiO₂ catalysts. The physicochemical properties of the catalysts are listed in Table 1. The Ru loadings on the catalysts are similar of about 10.5 wt%. The dispersion of Ru remained virtually constant at approximate 25% irrespective of the kinds of supports. The N₂ adsorption–desorption isotherms of the catalysts (Fig. S2) are analogous to the corresponding supports, while the S_{BET} and V_{pore} of the catalysts are higher and the d_{pore} is lower than those of the corresponding supports owing to the deposition of the Ru NPs. Fig. 3 displayed the XRD patterns of the Ru/TiO₂ catalysts. After Ru loading, the crystallographic form of the TiO₂ samples was retained. Meanwhile, an extra weak and diffuse feature appeared at ca. 44°, attributing to the (1 0 1) diffraction of the hexagonally close packed (hcp) Ru [12]. This weak and diffuse feature was originated from the high dispersion and small size of Ru on the Ru/TiO₂ catalysts, as indicated by CO chemisorption results (Table 1) and TEM images shown below.

Fig. 4a exhibited the SEM image of the Ru/TiO₂-453 catalyst. It is obvious that the morphology of TiO₂ remained perfectly after the loading of Ru NPs, while the facets became rough. The distribution of Ru on TiO₂ was observed by the energy-dispersive X-ray (EDX) elemental mapping analysis with corresponding high angle annular dark field-scanning transmission electron microscopy (HAADF-STEM) image (Fig. 4b). It is clear that the Ru NPs were uniformly distributed in the entire region. Fig. 4c presents the TEM image, SAED pattern, and particle size distribution (PSD) histogram with Gaussian analysis fitting of the Ru/TiO₂-453 catalyst. In this figure, the Ru NPs verified by EDX shown in Fig. S3c were evenly distributed on the (1 0 0) planes of TiO₂, and the mean size is 3.4 nm with a PSD ranging in 2–5 nm. The SAED pattern inset in Fig. 4c shows diffraction rings and random dots, corresponding to the diffraction of the Ru NPs and TiO₂, respectively, which agreed with the short-range ordered and long-range disordered atomic arrangement of the Ru NPs prepared by the chemical reduction method [24]. The HRTEM image in Fig. 4d provides more structural details of the Ru/TiO₂-453 catalyst. The lattice fringes with the interplanar spacings of approximate 2.05 and 3.52 Å ascribable to the (1 0 1) planes of hcp Ru and TiO₂, respectively, were visible, which were further confirmed by the fast Fourier transform (FFT) pattern inset in Fig. 4d.

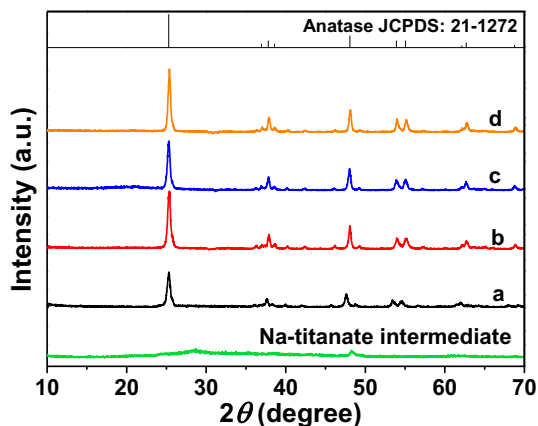


Fig. 1. XRD patterns of Na-titanate intermediate and (a) TiO₂-433, (b) TiO₂-443, (c) TiO₂-453, and (d) TiO₂-473.

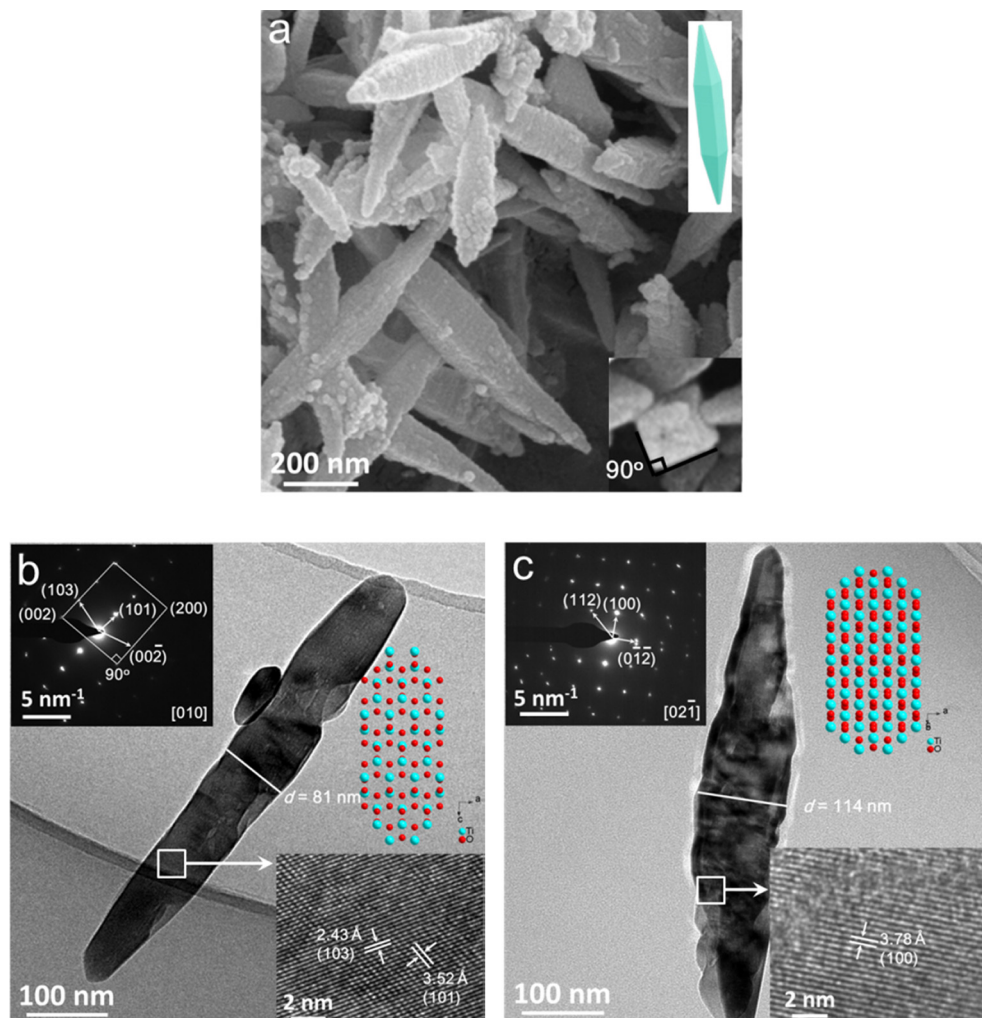


Fig. 2. (a) SEM image of TiO₂-453. The inset is the top view of a single TiO₂ nanorod; (b) TEM image of an individual nanorod of TiO₂-453 viewed along the [0 1 0] direction. The insets are the corresponding SEAD pattern, schematic model of an ideal nanorod projected along the [0 1 0] direction, and HRTEM image taken from the nanorod indicated by the rectangle; (c) TEM image of an individual nanorod of TiO₂-453 viewed along the [0 2 1] direction. The insets are the corresponding SEAD pattern, schematic model of an ideal nanorod projected along the [0 2 1] direction, and HRTEM image taken from the nanorod indicated by the rectangle.

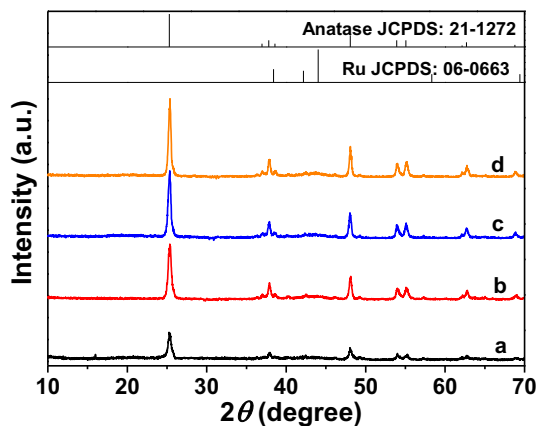


Fig. 3. XRD patterns of the (a) Ru/TiO₂-433, (b) Ru/TiO₂-443, (c) Ru/TiO₂-453, and (d) Ru/TiO₂-473 catalysts.

For the Ru/TiO₂-433, Ru/TiO₂-443, and Ru/TiO₂-473 catalysts, the SEM images (Fig. 5a1–c1) showed that the morphologies of TiO₂ are nonuniform than that of the Ru/TiO₂-453 catalyst, evidencing the crucial role of the hydrothermal temperature for pro-

ducing the ideal TiO₂ nanorods with dominated {1 0 0} facets. Excessively low temperature resulted in the partial formation of the nanorods (Fig. 5a1), while too high temperature led to the aggregation of the nanorods and consequently, the nanorods became irregular (Fig. 5c1). The optimum temperature for obtaining the perfect nanorods is 453 K. Fig. 5a2–c2 indicated that the Ru NPs verified by EDX shown in Fig. S3 were uniformly distributed on the supports, which was further proved by the EDX elemental mapping analysis (Fig. S4). The average sizes of the Ru NPs are identical of 3.3 nm and the PSD ranges are similar of 2–5 nm, which is qualitatively in agreement with the results of CO chemisorption. The SAED patterns of the Ru/TiO₂-433, Ru/TiO₂-443, and Ru/TiO₂-473 catalysts are also similar to that of the Ru/TiO₂-453 catalyst. The HRTEM images of these catalysts shown in Fig. 5a3–c3 indicated that the Ru NPs are approximately spherical and in close contact with the supports. The lattice fringes on the Ru NPs had the same interplanar spacings of approximate 2.05 Å, ascribing to the (1 0 1) planes of *hcp* Ru. The short-range ordered and long-range disordered feature of these lattice fringes embodied the amorphous alloy structure of the Ru NPs [24]. Moreover, the lattice fringes with the interplanar spacings of approximate 2.43, 3.52, and 2.38 Å were visualized for the Ru/TiO₂-433, Ru/TiO₂-443, and Ru/TiO₂-473 catalysts, respectively, attributing to the (1 0 3), (1 0 1), and (0 0 4) planes of TiO₂.

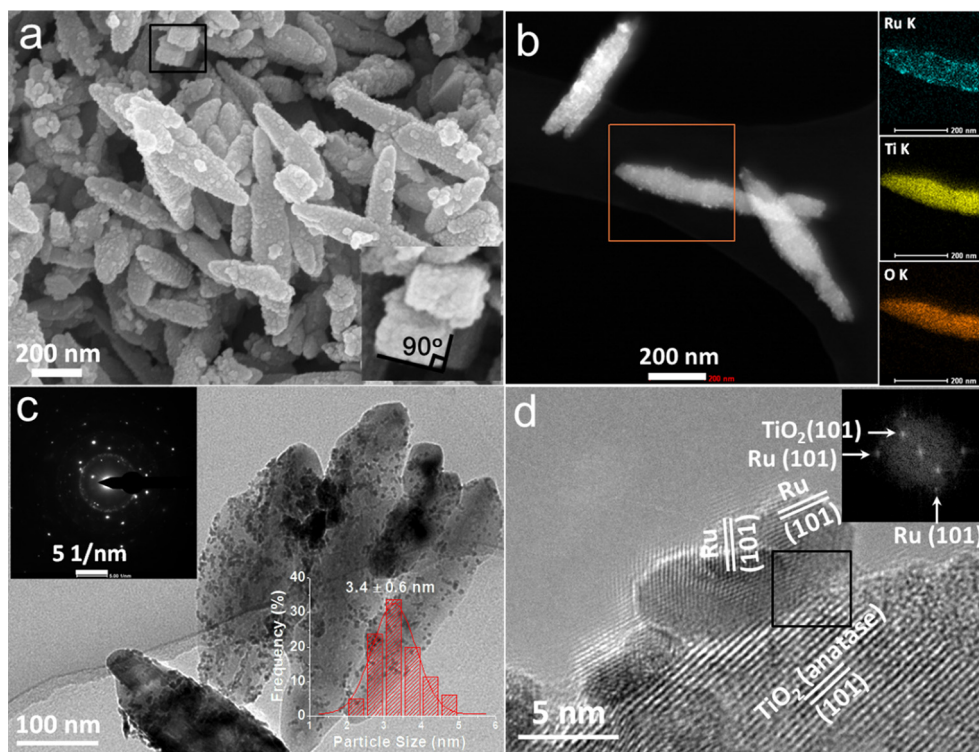


Fig. 4. (a) SEM image with the top view of a single nanorod indicated by the rectangle, (b) mapping EDX and corresponding HAADF-STEM image, (c) TEM image with the corresponding PSD histogram of the Ru NPs with Gaussian analysis fitting and SAED image, and (d) HRTEM image with FFT pattern indicated by the rectangle of the Ru/TiO₂-453 catalyst.

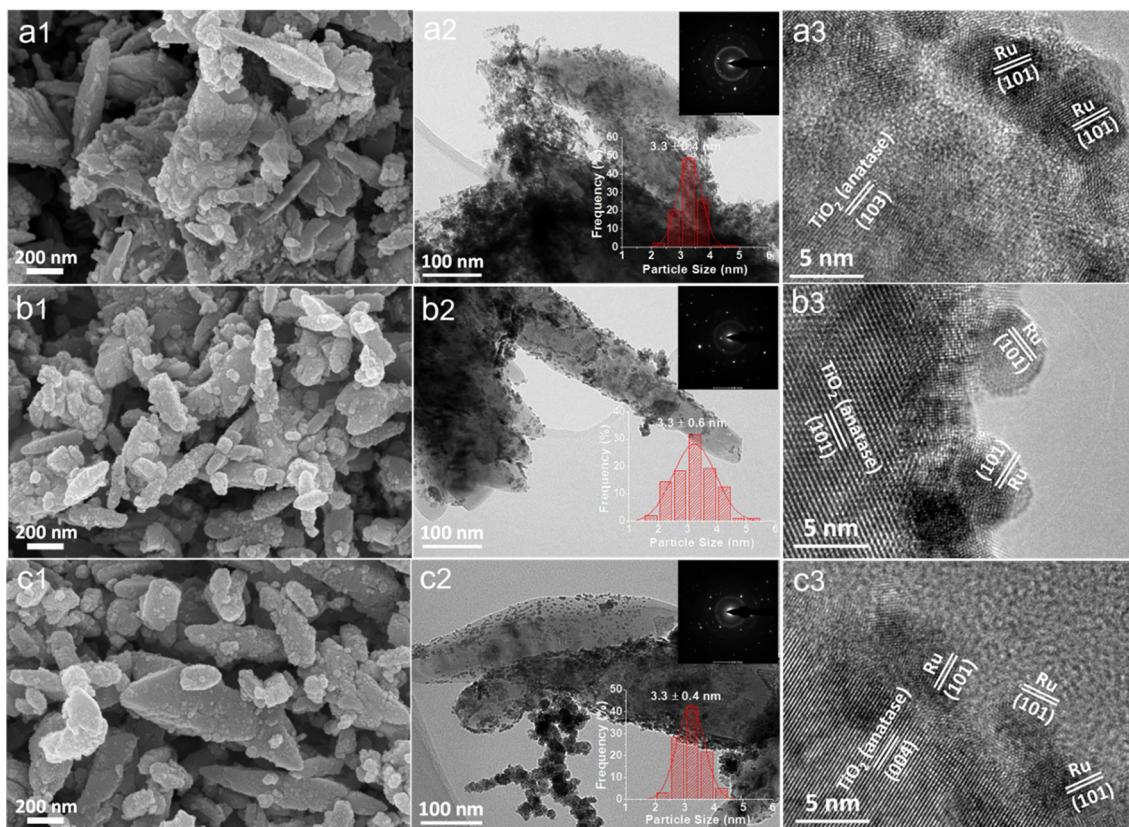


Fig. 5. SEM images (left), TEM images with the corresponding PSD histograms of the Ru NPs with Gaussian analysis fittings and SAED images (middle), and HRTEM images (right) of the (a1–a3) Ru/TiO₂-433, (b1–b3) Ru/TiO₂-443, and (c1–c3) Ru/TiO₂-473 catalysts.

3.3. Chemical state and hydrophilicity of the Ru/TiO₂ catalysts

Fig. 6 displays the Ru3p and Ti2p spectra of the Ru/TiO₂-433, Ru/TiO₂-443, Ru/TiO₂-453, and Ru/TiO₂-473 catalysts. In consideration of the partly overlapping between the Ru3p_{3/2} and Ti2p peaks, the deconvolution of the spectra is conducted to ascertain the relative contributions. For all four catalysts, the Ti2p spectrum exhibited two peaks at 458.8 eV (Ti 2p_{3/2}) and 464.5 eV (Ti 2p_{1/2}), assigning to Ti⁴⁺ oxidation state [25]. The Ru3p_{1/2} BE and the 3p_{3/2}–3p_{1/2} doublet separation are 484.1 eV and 22.1 eV, respectively, evidencing the metallic Ru [25]. This assignment can be further confirmed by the Ru3d spectra shown in Fig. S5, since the Ru3d_{5/2} BE and the 3d_{5/2}–3d_{3/2} doublet separation are 280.1 eV and 4.2 eV, respectively, for the four catalysts. The Ru/Ti surface molar ratios of the Ru/TiO₂ catalysts originated from Fig. 6 are listed in Table 2. All four catalysts exhibited a higher Ru/Ti surface molar ratio than the corresponding bulk one, signifying a surface segregation of Ru.

As pointed out by Li et al. [6], in the preparation of TiO₂ nanorods, the OH[−] released from Na-titanate intermediates would preferentially adsorb onto {1 0 0} facets of anatase TiO₂. We inferred that this OH[−] adsorption would increase the hydrophilicity of TiO₂ nanorod with dominated {1 0 0} facets, and subsequently increasing the hydrophilicity of the Ru/TiO₂ catalyst. To verify this assumption, FTIR and water contact angle analyses were carried out. In Fig. S6, the FTIR spectra of the TiO₂ samples after saturation adsorption of H₂O are exhibited. The weak band at 2353 cm^{−1} is probably assigned to carbonaceous contaminants. The broad and strong band at 3473 cm^{−1} is assigned to the stretching vibration of hydrogen-bonded OH groups [26]. This band was increased in intensity when the hydrothermal temperature increased from 433 K to 453 K, and then weakened at 473 K. The integral band intensity obeyed the order of TiO₂-433 < TiO₂-473 < TiO₂-443 < TiO₂-453. Meanwhile, the integral intensity of the band at 1649 cm^{−1} attributable to the bending vibration of intact water exhibited the same sequence as that of the band at 3473 cm^{−1}. After the loading of Ru NPs, the integral intensity order of the band at 3460 cm^{−1} remained unchanged (Fig. 7A). The water contact angle of the Ru/TiO₂ catalysts inserted in Fig. 7A evolved in the order of Ru/TiO₂-433 > Ru/TiO₂-473 > Ru/TiO₂-443 > Ru/TiO₂-453, further demonstrating the contrary hydrophilicity sequence of the Ru/TiO₂ catalysts. The variation in the hydrophilicity of the Ru/TiO₂ catalysts can be interpreted by O1s XPS analysis. As shown in Fig. 7B, the deconvolution of the O1s spectra afforded three peaks at 530.1, 531.9, and 533.1 eV, attributing to lattice oxygen in TiO₂ (O_L), oxygen in hydroxyl groups (O_{OH}), and oxygen in H₂O (O_{H2O}), respectively [27,28]. The O_{OH}/Ti surface molar ratios are

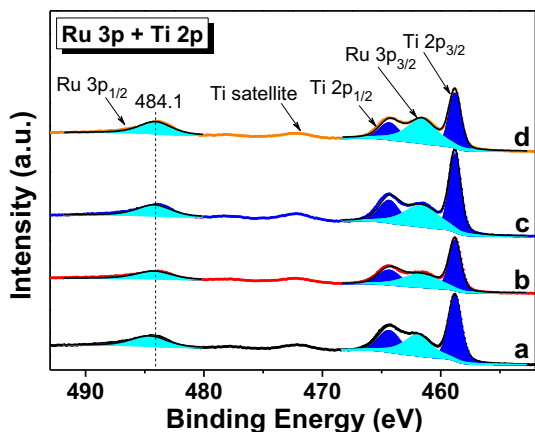


Fig. 6. The Ru3p and Ti2p spectra of the (a) Ru/TiO₂-433, (b) Ru/TiO₂-443, (c) Ru/TiO₂-453, and (d) Ru/TiO₂-473 catalysts.

Table 2

XPS results of the Ru/TiO₂ catalysts.

Catalyst	Ru/Ti surface molar ratio ^a	O _{OH} /Ti molar ratio ^b
Ru/TiO ₂ -433	1.18 (0.075)	0.48
Ru/TiO ₂ -443	1.29 (0.075)	0.62
Ru/TiO ₂ -453	1.29 (0.075)	0.68
Ru/TiO ₂ -473	1.88 (0.076)	0.60

^a Data in parentheses are the bulk molar ratios determined by inductively coupled plasma-atomic emission spectroscopy (ICP-AES).

^b O_{OH}, surface hydroxyl.

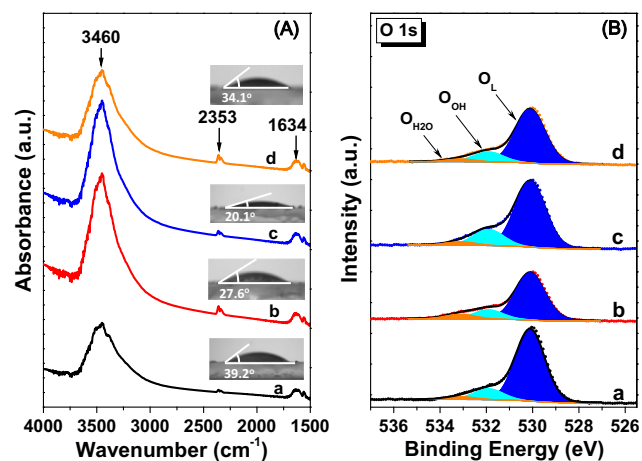


Fig. 7. (A) The FTIR spectra obtained at 298 K of the (a) Ru/TiO₂-433, (b) Ru/TiO₂-443, (c) Ru/TiO₂-453, and (d) Ru/TiO₂-473 catalysts. Insets are the corresponding water contact angles; (B) The O1s spectra of the (a) Ru/TiO₂-433, (b) Ru/TiO₂-443, (c) Ru/TiO₂-453, and (d) Ru/TiO₂-473 catalysts.

summarized in Table 2. It is obvious that the Ru/TiO₂-453 catalyst with the highest exposed degree of {1 0 0} facets on TiO₂ possessed the highest O_{OH}/Ti ratio, verifying that the OH[−] released from Na-titanate intermediates would preferentially adsorb onto the {1 0 0} facets of TiO₂ and subsequently increase the hydrophilicity of the Ru/TiO₂ catalyst. The O_{OH}/Ti surface molar ratios increased in the sequence of Ru/TiO₂-433 < Ru/TiO₂-473 < Ru/TiO₂-443 < Ru/TiO₂-453, conforming with the hydrophilicity sequence disclosed by the FTIR and water contact angle characterizations.

3.4. Acidity of the Ru/TiO₂ catalysts

Exposure of Lewis and Brønsted acid sites on oxide surface is an essential demand for adsorption of reactive molecules and catalytic application. FTIR spectroscopy of adsorbed small alkaline molecules, such as pyridine, NH₃, CO, CH₃CN, or NO, is widely recognized as a powerful technique to characterize the nature and concentration of acid sites. As an IR probe molecule, pyridine is superior to others in terms of higher selectivity and stability than NH₃, stronger adsorption than CO and CH₃CN, and relatively higher sensibility to the strength of acid sites than NO [29]. Hence, FTIR of adsorbed pyridine (Py-IR) characterization was conducted to investigate the nature and concentration of acid sites on the Ru/TiO₂ catalysts. According to previous works [29–32], various vibration bands of pyridine originated from different adsorption sites appeared at around 1446 (Lewis acid sites-coordinated pyridine, L-Py), 1491 (ring vibration of adsorbed pyridine), 1581 (hydrogen bonded pyridine, hb-Py), and 1596 cm^{−1} (strong L-Py) in Py-IR spectrum of TiO₂ at room temperature. If the concentration of acid sites needs to be evaluated, the IR spectra should be recorded at 423 K to eliminate the physically adsorbed pyridine [30].

On basis of the above results, we collected the Py-IR spectra of the Ru/TiO₂ catalysts at 423 K, as shown in Fig. 8. Interestingly, differing from the previous observation that only the Lewis acid sites existed on TiO₂ [30,33], an additional band at 1545 cm⁻¹ attributing to Brønsted acid sites-coordinated pyridine appeared for all the catalysts. According to Arrouvel et al. [34], a rather high amount of OH groups, which represented the Brønsted acid sites, will generate on the (1 0 0) surface of anatase TiO₂ when it was hydrotreated. Therefore, the origin of the Brønsted acid sites on the Ru/TiO₂ catalysts can be assigned to the OH groups on the {1 0 0} facets of TiO₂ as corroborated by O1s spectra. By integrating the intensity of the bands at 1446 and 1545 cm⁻¹, the amounts of Lewis acid sites (n_{L-Py}) and Brønsted acid sites (n_{PyH^+}), as well as the total amount of acid sites determined by Py-IR (n_{Py}) were calculated, as shown in Table 3. It is obvious that the n_{PyH^+} and n_{Py} of the Ru/TiO₂ catalysts decreased with the elevation of the hydrothermal temperature.

The effect of the exposed degree of the {1 0 0} facets of TiO₂ on the amount and strength of the acid sites on the Ru/TiO₂ catalysts was further investigated by temperature-programmed desorption (TPD) of NH₃ (NH₃-TPD), as displayed in Fig. 9. A similar three peak-profile at 452, 666, and 791 K attributing to NH₃ adsorbed on weak acid sites, acid sites with medium strength, and strong acid sites [35], respectively, was exhibited for all four catalysts, suggesting that the exposed degree of the {1 0 0} facets of TiO₂ had no impact on the strength of the acid sites. However, the peak intensity of the desorbed NH₃ decreased with the elevation of the hydrothermal temperature. By integrating the peak areas, the overall amounts of acid sites (n_{NH_3}) were calculated and displayed in Table 3. It is evident that the NH₃-TPD and Py-IR matched well on the variation of the acid amounts, and the observation that n_{NH_3} is always higher than n_{Py} is in line with the smaller kinetic diameter and higher basicity of NH₃ than pyridine.

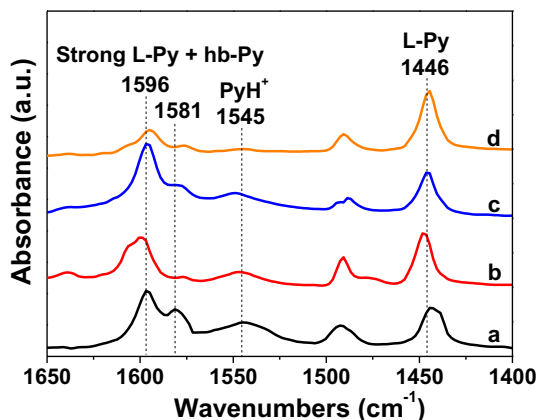


Fig. 8. Py-IR spectra of the (a) Ru/TiO₂-433, (b) Ru/TiO₂-443, (c) Ru/TiO₂-453, and (d) Ru/TiO₂-473 catalysts at 423 K. The spectra had been normalized by sample mass.

Table 3

The acidic properties of the Ru/TiO₂ catalysts.

Catalyst	A_{L-Py}^a (cm ⁻¹ g ⁻¹)	$A_{PyH^+}^b$ (cm ⁻¹ g ⁻¹)	n_{L-Py}^c (μmol g ⁻¹)	$n_{PyH^+}^d$ (μmol g ⁻¹)	n_{Py}^e (μmol g ⁻¹)	$n_{NH_3}^f$ (μmol g ⁻¹)
Ru/TiO ₂ -433	163	111	231	209	440	2965
Ru/TiO ₂ -443	179	75	253	141	394	1412
Ru/TiO ₂ -453	150	47	212	88	300	1386
Ru/TiO ₂ -473	201	7	284	13	297	1319

^a The integral absorption band intensity of Lewis acid sites-bonded pyridine (L-Py) at 1446 cm⁻¹ in the Py-IR spectra collected at 423 K.

^b The integral absorption band intensity of Brønsted acid sites-bonded pyridine (PyH⁺) at 1545 cm⁻¹ in the Py-IR spectra collected at 423 K.

^c The amount of pyridine adsorbed on Lewis acid sites determined by Py-IR.

^d The amount of pyridine adsorbed on Brønsted acid sites determined by Py-IR.

^e The total amount of pyridine adsorbed on Lewis and Brønsted acid sites determined by Py-IR.

^f The amount of desorbed NH₃ determined by NH₃-TPD.

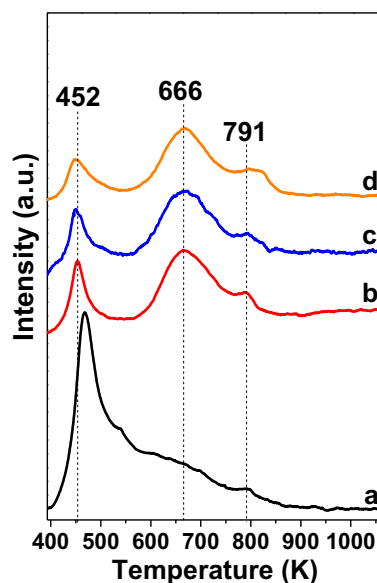
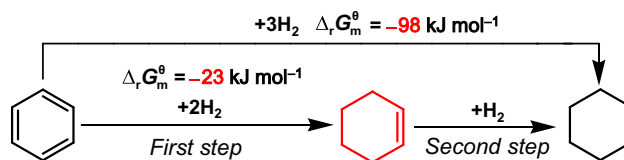


Fig. 9. NH₃-TPD profiles of the (a) Ru/TiO₂-433, (b) Ru/TiO₂-443, (c) Ru/TiO₂-453, and (d) Ru/TiO₂-473 catalysts.



Scheme 2. The pathway and thermodynamics of benzene hydrogenation.

3.5. Selective hydrogenation of benzene to cyclohexene

Owing to the reactive C=C bond, cyclohexene molecules are readily converted to highly value-added chemicals such as cyclohexanol, adipic acid, and caprolactam by conventional olefin reactions. However, the achievement of a high cyclohexene yield from the environmentally toxic feedstock-eliminated, atom-economic, and operation-simplified route of benzene hydrogenation is severely restricted to thermodynamics, that is, the standard free energy change for the formation of complete hydrogenation product (cyclohexane) from benzene hydrogenation (-98 kJ mol^{-1}) is more negative than that of the formation of intermediate cyclohexene (-23 kJ mol^{-1}) [36,37], as shown in Scheme 2. Besides, first-principles calculations substantiated that the energy barrier of the first hydrogenation step is higher than that of the second step even on the most selective Ru metal [38]. These limitations resulted in the relatively low cyclohexene yield on a majority of reported Ru-based catalysts.

Remarkably, Fig. 10 shows that the regulation of the facets of TiO₂ support is an efficient approach for Ru to break through these limitations. As illustrated in Fig. 10, the desired intermediate cyclohexene and the by-product cyclohexane are the only detected products. The benzene content decreased and the cyclohexane content increased monotonically as the reaction proceeded. For the cyclohexene content, a maximum appeared at a certain reaction time, which conformed with the known feature of the consecutive reaction. Among the four catalysts, the Ru/TiO₂-433 catalyst exhibited the lowest cyclohexene yield of 21%, while the reaction proceeded the fastest that only 45 min was required to convert 90% of benzene. A dramatical increment for the cyclohexene yield appeared on the Ru/TiO₂-443 catalyst (52%). On the Ru/TiO₂-453 catalyst, cyclohexene amounted to the highest yield of 54%, and then declined to 40% on the Ru/TiO₂-473 catalyst. Additionally,

the curve of the cyclohexene selectivity against the benzene conversion of the optimal Ru/TiO₂-453 catalyst at the third run perfectly mimics the first run (Fig. S7), manifesting the good stability of the catalyst.

Table 4 lists the catalytic results of the selective hydrogenation of benzene on the Ru/TiO₂ catalysts. The r_0 decreased gradually with the elevation of the hydrothermal temperature of TiO₂. According to the r_0 and the dispersion data in Table 1, the TOFs of benzene were calculated. It is observed that the TOFs showed the same decreased tendency with the r_0 . The highest TOF of the Ru/TiO₂-433 catalyst was close to that of the Ru/anatase catalyst we reported previously [39].

As the particle size and chemical state of the Ru NPs on the Ru/TiO₂ catalysts were similar, it is reasonable to exclude the possibility that the Ru NPs caused the difference in the TOFs.

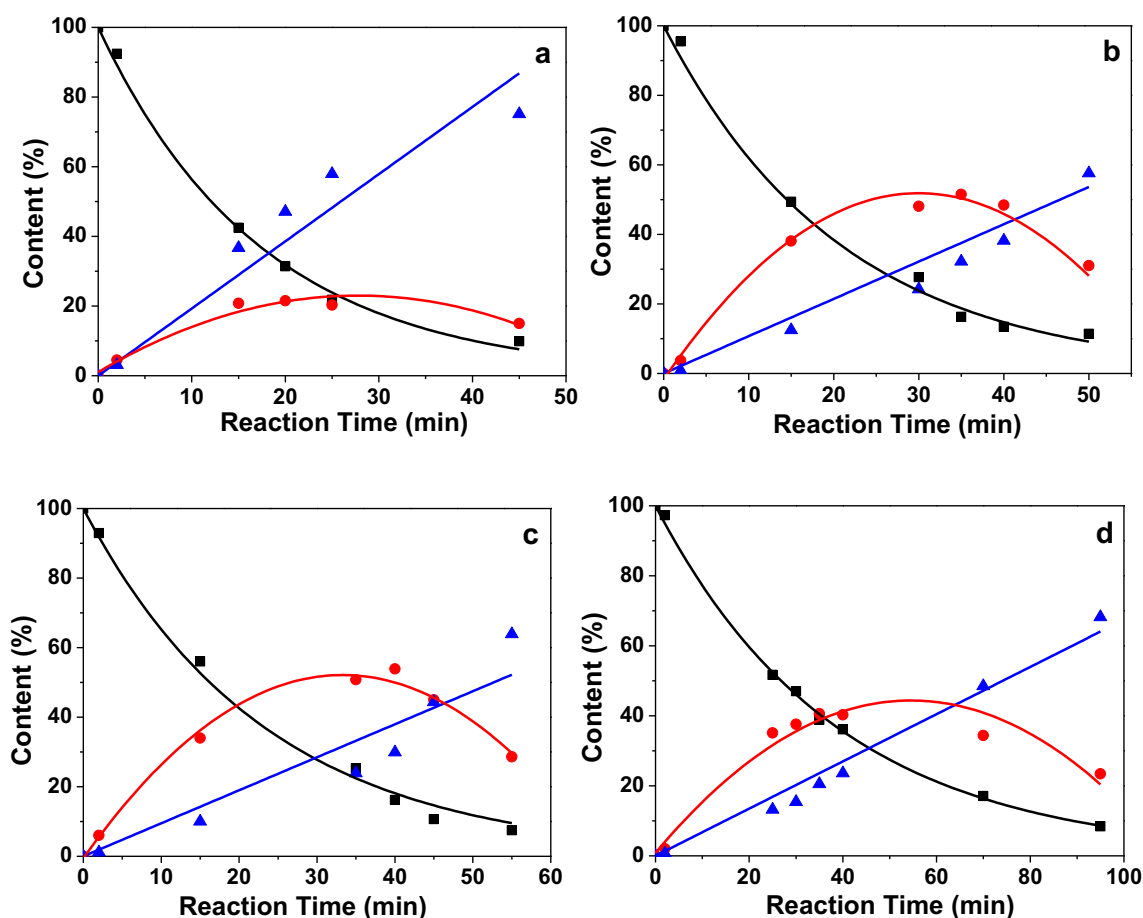


Fig. 10. The time courses of benzene hydrogenation over the (a) Ru/TiO₂-433, (b) Ru/TiO₂-443, (c) Ru/TiO₂-453, and (d) Ru/TiO₂-473 catalysts. Reaction conditions: 0.5 g of catalyst, 25 ml of benzene, 50 ml of H₂O, 5.0 g of ZnSO₄·7H₂O, temperature of 413 K, H₂ pressure of 5.0 MPa, and stirring rate of 1200 rpm. (■) benzene, (●) cyclohexene, and (▲) cyclohexane.

Table 4
Results of the selective hydrogenation of benzene over the Ru/TiO₂ catalysts.^a

Catalyst	t^b (min)	Conv. ^b (%)	S_{CHE}^b (%)	Y_{CHE}^b (%)	S_0^c (%)	r_0^d	TOF (min ⁻¹)
Ru/TiO ₂ -433	20	69	31	21	61	26.5	98.9
Ru/TiO ₂ -443	35	84	62	52	87	19.7	76.9
Ru/TiO ₂ -453	40	84	64	54	93	15.8	58.0
Ru/TiO ₂ -473	40	64	63	40	77	11.7	44.1

^a Reaction conditions: 0.5 g of catalyst, 25 ml of benzene, 50 ml of H₂O, 5.0 g of ZnSO₄·7H₂O, temperature of 413 K, H₂ pressure of 5.0 MPa, and stirring rate of 1200 rpm.

^b Values recorded at the maximum yield of cyclohexene.

^c Initial selectivity towards cyclohexene.

^d Initial weight specific activity, unit in mmol_{C₆H₆} g_{cat}⁻¹ min⁻¹.

We previously identified that the additional hydrogenation between adsorbed benzene molecules and spillover hydrogen (H_{so}) from metal sites was existed on the acid sites of supports of the Ru/B-ZrO₂ and Ru/AlOOH-SiO₂ catalysts, which improved the TOF of benzene [12,23]. For the anatase TiO₂ supported-Ru₁₀ clusters, Chen et al. found that the adsorbed H₂ molecules on the metal cluster became thermodynamically favorable to dissociate and spill onto the support surface at high hydrogen coverage [40]. Analogously, in the light of the close contact between Ru NPs and TiO₂ surfaces on the Ru/TiO₂ catalysts revealed by HRTEM and the high H₂ pressure (5.0 MPa) in reaction, it is rational to infer that in benzene hydrogenation over the Ru/TiO₂ catalysts, the H₂

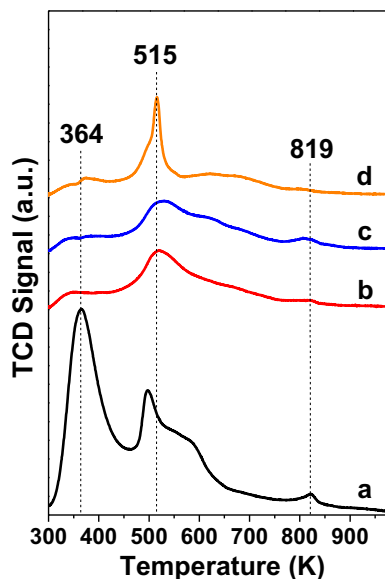


Fig. 11. The TPD profiles of benzene on the (a) Ru/TiO₂-433, (b) Ru/TiO₂-443, (c) Ru/TiO₂-453, and (d) Ru/TiO₂-473 catalysts.

molecules adsorbed on the Ru NPs would dissociate and spill onto the TiO₂ surfaces, generating the H_{so} species.

On the other hand, we investigated the adsorption capacity of benzene on the Ru/TiO₂ catalysts by TPD, as shown in Fig. 11. A similar three peak-profile was exhibited for all four catalysts. The peak at 364 K was attributed to the residual physisorbed benzene as the desorption temperature approached to the boiling point of benzene. The peaks at 515 and 819 K are assigned to chemisorbed benzene. The integral peak intensity of the chemisorbed benzene decreased with the elevation of the hydrothermal temperature, which is consistent with the decrement in the amount of acid sites (Table 3). This variation should be originated from the adsorption of benzene on the acid sites of TiO₂ supports since Lin et al. [41] and Simon et al. [42] demonstrated that aside from the adsorption of benzene on the Ru NPs, benzene can also adsorb on the Lewis and Brønsted acid sites of supports. In addition, when plotting the natural logarithm of benzene concentration with the t derived from Fig. 10, a good linear relationship was emerged (Fig. S8), revealing that the reaction is first order relative to benzene. Therefore, the higher the hydrothermal temperature of TiO₂ is, the less the benzene adsorbed on the acid sites reacting with H_{so} that is also adsorbed on TiO₂, and as a result, a lower TOF. By plotting the TOFs with the n_{py} in Table 3, an excellent linearity appeared in Fig. 12A, further verifying the acid sites-induced activity enhancement for the Ru/TiO₂ catalysts.

3.6. Implications of the TiO₂ facets on the cyclohexene selectivity

As the hydrothermal temperature of TiO₂ elevated, an firstly increased and then declined tendency emerged for the S_0 (Table 4). Meanwhile, it is delighted that supporting the Ru NPs on anatase TiO₂ with the highest degree of exposed {1 0 0} facets significantly promoted the cyclohexene selectivity: the S_0 on the Ru/TiO₂-453 catalyst attained to 93%, which is higher than that of our previously reported Ru/anatase catalyst (82%) [39], as well as the Ru/Al₂O₃, Ru/SiO₂, Ru/CoO, Ru/NiO, Ru/CuO, and Ru/ZnO catalysts

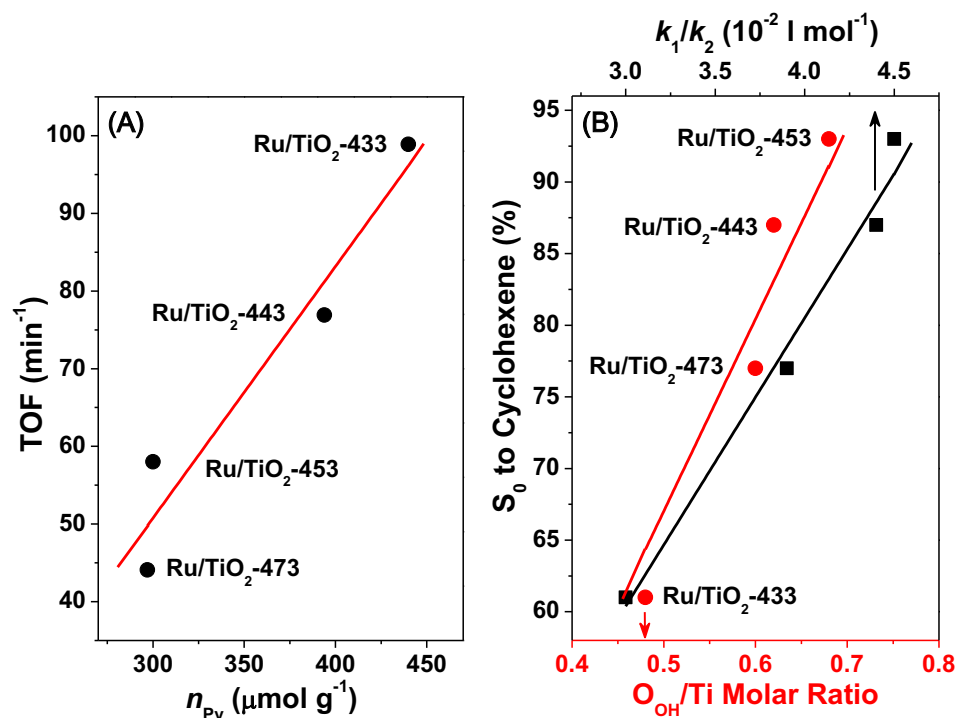


Fig. 12. (A) Correlation of TOF and n_{py} , and (B) correlation of S_0 and the O_{OH}/Ti molar ratio and k_1/k_2 ratio on the Ru/TiO₂ catalysts.

(Table S1). According to our previous work [23], the acid sites on the support of the Ru/B-ZrO₂ catalyst affected the cyclohexene selectivity by altering the rates of the two hydrogenation steps shown in Scheme 2. To examine the validity of this viewpoint on the Ru/TiO₂ catalysts, the rate constants of these two steps (k_1 and k_2) were calculated from the slopes of the linearities between the natural logarithm of benzene concentration ($\ln[C_6H_6]$) against t as well as the cyclohexane concentration ($[C_6H_{12}]$) against t based on the reaction data shown in Fig. 10 and the rate equations raised by Liu et al. [43], that is, $\ln[C_6H_6] = \ln[C_6H_6]_0 - k_1 t$ and $[C_6H_{12}] = k_2 t$, in which $[C_6H_6]_0$ is initial benzene concentration. As summarized in Table 5, both k_1 and k_2 decreased with the elevation of the hydrothermal temperature, while the degrees of the decrements were different. The evolutionary process of the k_1/k_2 ratio matched with that of the S_0 , evidencing the validity of the above acid sites-selectivity relationship. By plotting the S_0 against the k_1/k_2 values, an excellent linearity appeared in Fig. 12B, which finely proves the significance of the acid sites on the enhancement of the cyclohexene selectivity by modifying the kinetics of benzene hydrogenation.

On the other hand, as discussed above, aside from the implication of the TiO₂ facets on the amount of acid sites, the amount of hydroxyl groups was also altered by the exposed degree of TiO₂ {1 0 0} facets, and as a result, the hydrophilicity of the Ru/TiO₂ catalysts was changed. For the benzene selective hydrogenation on Ru-based catalysts, Struijk et al. corroborated that the H₂O layer formed on the catalyst surface was vital for the improvement of the cyclohexene selectivity by (i) occupying the active sites where cyclohexane is preferentially generated, and (ii) promoting the desorption of cyclohexene from the catalyst surface and inhibiting its readsorption [44,45]. Therefore, as illustrated in Scheme 3, the catalyst with more surface OH groups rendered the higher amount of adsorbed H₂O in benzene hydrogenation, and thereby the selec-

tivity towards cyclohexene is higher. A well linear relationship was established when correlating the S_0 and O_{OH}/Ti surface ratio originated from the O1s spectra (Fig. 12B), further manifesting the crucial role of the hydrophilicity of the Ru/TiO₂ catalysts in benzene selective hydrogenation. In agreement with this explanation, Peng et al. found that Ru supported on ZrO₂ heterophase structure nanocrystal consisting of both monoclinic and tetragonal phases was more efficient than which on single-phase ZrO₂, attributing to the higher concentration of the surface OH groups on the former catalyst [46]. Spod et al. detected the formation of Zn(OH)₂ during benzene selective hydrogenation over the Ru/La₂O₃-ZnO catalyst, which improved the hydrophilicity of the catalyst and consequently, promoted the cyclohexene yield [47]. Yu et al. observed a significant increment in cyclohexene selectivity of the Ru@TiO₂ catalyst when comparing with that of bare Ru, owing to the suppressed diffusion of cyclohexene onto Ru particles by the hydrophilic coating film [48]. Wang et al. discovered that more structural H₂O and surface OH groups were existed on the RuB/Al₂O₃·xH₂O catalyst than on the RuB/γ-Al₂O₃ catalyst, which improved the hydrophilicity and accordingly the cyclohexene yield [49].

In addition to the role of the OH groups on the TiO₂ {1 0 0} facets in stabilizing the stagnant H₂O layer on the Ru/TiO₂ catalysts, we investigated the direct interaction of cyclohexene with the OH groups by cyclohexene TPD, employing the Ru/TiO₂-433 and Ru/TiO₂-453 catalysts as representatives. As shown in Fig. 13, four desorption peaks at 366, 511, 539, and 825 K appeared on the Ru/TiO₂-433 catalyst, while only three peaks at 366, 529, and 825 K were existed on the Ru/TiO₂-453 catalyst. The peak at 366 K can be assigned to the residual physisorbed cyclohexene since the desorption temperature is close to the boiling point of cyclohexene, and other peaks were assigned to chemisorbed cyclohexene. One less desorption peak on the Ru/TiO₂-453 catalyst demonstrated that the surface OH groups decreased the type of adsorption sites. Simultaneously, although the intensity of the peak at 825 K slightly increased for the Ru/TiO₂-453 catalyst, the peak at 529 K was dramatically attenuated, revealing that the OH groups can also block the adsorption sites for cyclohexene. As mentioned above, first-principles calculations testified that the hydrogenation energy barrier of benzene to cyclohexene is higher than

Table 5
The rate constants for the hydrogenation of benzene to cyclohexene (k_1) and cyclohexene to cyclohexane (k_2) over the Ru/TiO₂ catalysts fitted from reaction data in Fig. 10 according to the kinetic equations raised by Ref. [43].

Catalyst	k_1 (10 ⁻² min ⁻¹)	k_2 (10 ⁻² mol l ⁻¹ min ⁻¹)	k_1/k_2 (10 ⁻² l mol ⁻¹)
Ru/TiO ₂ -433	5.7	193	3.0
Ru/TiO ₂ -443	4.7	107	4.4
Ru/TiO ₂ -453	4.3	95	4.5
Ru/TiO ₂ -473	2.6	67	3.9



Scheme 3. Schematic illustration of the mechanism of benzene selective hydrogenation over the Ru/TiO₂ catalysts.

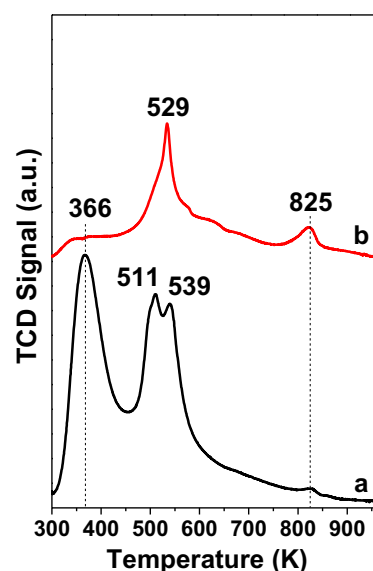


Fig. 13. The TPD profiles of cyclohexene on the (a) Ru/TiO₂-433 and (b) Ru/TiO₂-453 catalysts.

cyclohexene to cyclohexane on the Ru(0 0 0 1) surface [38]. This signifies that cyclohexene will be facily saturated once it was formed on the catalyst. Therefore, the decreased type of adsorption sites and the suppressed adsorption of cyclohexene on the Ru/TiO₂-453 catalyst by more surface OH groups derived from higher exposed degree of TiO₂ {1 0 0} facets may be additionally critical factors for the remarkable selectivity enhancement in benzene selective hydrogenation.

4. Conclusions

This work presents a comprehensive study on the support facet effect of the Ru/TiO₂ catalysts for benzene selective hydrogenation to cyclohexene. Anatase TiO₂ nanorods exposed different degrees of {1 0 0} facets were successfully synthesized by hydrothermal route at different temperatures, in which 453 K is identified to be the optimal temperature for exposing the most {1 0 0} facets. It is found that the increment of the exposed degree of TiO₂ {1 0 0} facets imposed no impact on the size, microstructure, and chemical state of the Ru NPs, but introduced more surface OH groups on the Ru/TiO₂ catalyst, resulting in improved hydrophilicity. Besides, the amount of acid sites on the Ru/TiO₂ catalysts decreased with the elevation of the hydrothermal temperature of supports. In benzene selective hydrogenation, the TOFs of benzene decreased gradually with the elevation of the hydrothermal temperature, while the cyclohexene selectivity displayed a volcanic-type evolution, passing through the highest initial selectivity of 93% and the maximum yield of 54% on the Ru/TiO₂-453 catalyst. The decrement in TOFs was attributed to the decreased amounts of acid sites on TiO₂ owing to that benzene can be additionally hydrogenated on the acid sites by H₂O. For the S₀ of cyclohexene, a positive linearity was established between which and the amount of OH groups, supporting the crucial character of the H₂O layer on the catalysts in determining the cyclohexene selectivity. In addition, we found that the surface OH groups can essentially suppress the cyclohexene adsorption by decreasing the type of adsorption sites and blocking the chemisorption sites, which is identified to be another key factor for the selectivity enhancement by support facet regulation. The intriguing support facet-performance relationship of the Ru/TiO₂ catalysts demonstrated in this work provides a new way for the design of more efficient Ru catalysts for benzene selective hydrogenation by regulating the facets of support other than TiO₂.

Acknowledgements

This work was supported by National Natural Science Foundation of China (No. 21703024), Natural Science Foundation of Chongqing, China (No. cstc2018jcyjAX0622, cstc2016jcyjA0392), and the Scientific and Technological Research Program of Chongqing Municipal Education Commission (No. KJ1500305).

Competing interests statement

There are no competing interests to declare.

Appendix A. Supplementary material

Supplementary data to this article can be found online at <https://doi.org/10.1016/j.jcat.2018.11.032>.

References

- [1] J. Pan, G. Liu, G.Q. Lu, H.M. Cheng, *Angew. Chem. Int. Ed.* 50 (2011) 2133–2137.
- [2] G. Longoni, R.L.P. Cabrera, S. Polizzi, M. D'Arienzo, C.M. Mari, Y. Cui, R. Ruffo, *Nano Lett.* 17 (2017) 992–1000.
- [3] M. Chen, J. Ma, B. Zhang, F. Wang, Y. Li, C. Zhang, H. He, *Appl. Catal. B: Environ.* 223 (2018) 209–215.
- [4] G. Liu, H.G. Yang, J. Pan, Y.Q. Yang, G.Q. Lu, H.M. Cheng, *Chem. Rev.* 114 (2014) 9559–9612.
- [5] L. Liu, Y. Jiang, H. Zhao, J. Chen, J. Cheng, K. Yang, Y. Li, *ACS Catal.* 6 (2016) 1097–1108.
- [6] J. Li, D. Xu, *Chem. Commun.* 46 (2010) 2301–2303.
- [7] B. Zhang, F. Wei, Q. Wu, L. Piao, M. Liu, Z. Jin, *J. Phys. Chem. C* 119 (2015) 6094–6100.
- [8] A. Beltrán, J.R. Sambrano, M. Calatayud, F.R. Sensato, J. Andrés, *Surf. Sci.* 490 (2001) 116–124.
- [9] Y. Sui, S. Liu, T. Li, Q. Liu, T. Jiang, Y. Guo, J.L. Luo, *J. Catal.* 353 (2017) 250–255.
- [10] M. Cao, Z. Tang, Q. Liu, Y. Xu, M. Chen, H. Lin, Y. Li, E. Gross, Q. Zhang, *Nano Lett.* 16 (2016) 5298–5302.
- [11] C. Liu, X.G. Han, S.F. Xie, Q. Kuang, X. Wang, M.S. Jin, Z.X. Xie, L.S. Zheng, *Chem. Asian J.* 8 (2013) 282–289.
- [12] G. Zhou, Y. Dong, L. Jiang, D. He, Y. Yang, X. Zhou, *Catal. Sci. Technol.* 8 (2018) 1435–1446.
- [13] S.J. Tauster, S.C. Fung, R.L. Garten, *J. Am. Chem. Soc.* 100 (1978) 170–175.
- [14] C. Wen, A.Y. Yin, Y.Y. Cui, X.L. Yang, W.L. Dai, K.N. Fan, *Appl. Catal. A: Gen.* 458 (2013) 82–89.
- [15] L.Y. Zou, Y.Y. Cui, W.L. Dai, *Chin. J. Chem.* 32 (2014) 257–262.
- [16] B. Wang, C. Wen, Y.Y. Cui, X. Chen, Y. Dong, W.L. Dai, *RSC Adv.* 5 (2015) 29040–29047.
- [17] X. Xue, J. Liu, D. Rao, S. Xu, W. Bing, B. Wang, S. He, M. Wei, *Catal. Sci. Technol.* 7 (2017) 650–657.
- [18] G. Zhou, H. Wang, J. Tian, Y. Pei, K. Fan, M. Qiao, B. Sun, B. Zong, *ChemCatChem* 10 (2018) 1184–1191.
- [19] Z. Peng, X. Liu, H. Lin, Z. Wang, Z. Li, B. Li, Z. Liu, S. Liu, *J. Mater. Chem. A* 4 (2016) 17694–17703.
- [20] D. Rao, X. Xue, G. Cui, S. He, M. Xu, W. Bing, S. Shi, M. Wei, *Catal. Sci. Technol.* 8 (2018) 236–243.
- [21] P. Zhang, T. Wu, T. Jiang, W. Wang, H. Liu, H. Fan, Z. Zhang, B. Han, *Green Chem.* 15 (2013) 152–159.
- [22] S.C. Hu, Y.W. Chen, *Ind. Eng. Chem. Res.* 36 (1997) 5153–5159.
- [23] G. Zhou, Y. Pei, Z. Jiang, K. Fan, M. Qiao, B. Sun, B. Zong, *J. Catal.* 311 (2014) 393–403.
- [24] Y. Pei, G. Zhou, N. Luan, B. Zong, M. Qiao, F. Tao, *Chem. Soc. Rev.* 41 (2012) 8140–8162.
- [25] J.F. Moulder, W.F. Stickle, P.E. Sobol, K.D. Bomben, *Handbook of X-ray Photoelectron Spectroscopy*, Perkin-Elmer, Minnesota, 1992.
- [26] H. Ishikawa, J.N. Kondo, K. Domen, *J. Phys. Chem. B* 103 (1999) 3229–3234.
- [27] Y. Zhu, L. Tian, Z. Jiang, Y. Pei, S. Xie, M. Qiao, K. Fan, *J. Catal.* 281 (2011) 106–118.
- [28] K. Lan, Y. Liu, W. Zhang, Y. Liu, A. Elzatahry, R. Wang, Y. Xia, D. Al-Dhayan, N. Zheng, D. Zhao, *J. Am. Chem. Soc.* 140 (2018) 4135–4143.
- [29] M.I. Zaki, M.A. Hasan, F.A. Al-Sagheer, L. Pasupulety, *Colloids Surf. A* 190 (2001) 261–274.
- [30] G. Zhou, Y. Dong, D. He, *Appl. Surf. Sci.* 456 (2018) 1004–1013.
- [31] P.A. Jacobs, C.F. Heylen, *J. Catal.* 34 (1974) 267–274.
- [32] I.S. Pieta, M. Ishaq, R.P.K. Wells, J.A. Anderson, *Appl. Catal. A: Gen.* 390 (2010) 127–134.
- [33] F. Liu, T. Wang, Y. Zheng, J. Wang, *J. Catal.* 355 (2017) 17–25.
- [34] C. Arrouvel, M. Digne, M. Breyssse, H. Toulhoat, P. Raybaud, *J. Catal.* 222 (2004) 152–166.
- [35] W.H. Chen, H.H. Ko, A. Sakthivel, S.J. Huang, S.H. Liu, A.Y. Lo, T.C. Tsai, S.B. Liu, *Catal. Today* 116 (2006) 111–120.
- [36] L. Foppa, J. Dupont, *Chem. Soc. Rev.* 44 (2015) 1886–1897.
- [37] H. Sun, Z. Chen, C. Li, L. Chen, Z. Peng, Z. Liu, S. Liu, *Catalysts* 8 (2018) 104–116.
- [38] C. Fan, Y.A. Zhu, X.G. Zhou, Z.P. Liu, *Catal. Today* 160 (2011) 234–241.
- [39] G. Zhou, R. Dou, H. Bi, S. Xie, Y. Pei, K. Fan, M. Qiao, B. Sun, B. Zong, *J. Catal.* 332 (2015) 119–126.
- [40] H.Y.T. Chen, S. Tosoni, G. Pacchioni, *ACS Catal.* 5 (2015) 5486–5495.
- [41] S.D. Lin, M.A. Vannice, *J. Catal.* 143 (1993) 539–553.
- [42] L.J. Simon, J.G. van Ommen, A. Jentys, J.A. Lercher, *Catal. Today* 73 (2002) 105–112.
- [43] S.C. Liu, Y.Q. Guo, X.L. Yang, Y.L. Ji, G. Luo, *Chin. J. Catal.* 24 (2003) 42–46.
- [44] J. Struijk, J.J.F. Scholten, *Appl. Catal. A: Gen.* 82 (1992) 277–287.
- [45] J. Struijk, M. Angremond, W.J.M. Regt, J.J.F. Scholten, *Appl. Catal. A: Gen.* 83 (1992) 263–295.
- [46] Z. Peng, X. Liu, S. Li, Z. Li, B. Li, Z. Liu, S. Liu, *Sci. Rep.* 7 (2017) 39847–39857.
- [47] H. Spod, M. Lucas, P. Claus, *ChemCatChem* 8 (2016) 2659–2666.
- [48] X.L. Yu, Y. Li, S.M. Xin, P.Q. Yuan, W.K. Yuan, *Ind. Eng. Chem. Res.* 57 (2018) 1961–1967.
- [49] J.Q. Wang, P.J. Guo, S.R. Yan, M.H. Qiao, H.X. Li, K.N. Fan, *J. Mol. Catal. A: Chem.* 222 (2004) 229–234.